Supplementary Information (SI) for EES Catalysis.

Supporting Information:

Vibrational Excitation in Plasma Catalysis: How Important are Dynamical Effects?

Floris van den Bosch* Nick Gerrits† Jörg Meyer‡

Leiden Institute of Chemistry, Gorlaeus Laboratories,

Leiden University, P.O. Box 9502, 2300 RA Leiden, The Netherlands

---

*f.van.den.bosch@lic.leidenuniv.nl
†n.gerrits@chem.leidenuniv.nl
‡j.meyer@chem.leidenuniv.nl

Contents

S1 Uncertainties of reaction probabilities

Figure S1 shows the dissociation probability curves obtained from our MD simulations together with the 95% confidence intervals due to extrapolation uncertainties in our high-dimensional neural network potential as described in Section 2.3.4 of the main article. These reaction curves are used for computing thermally-averaged reaction rate coefficients according to Eq. (6), mean vibrational efficacy as shown in Section S4, and energy-dependent vibrational efficacy curves shown in Fig. 3.

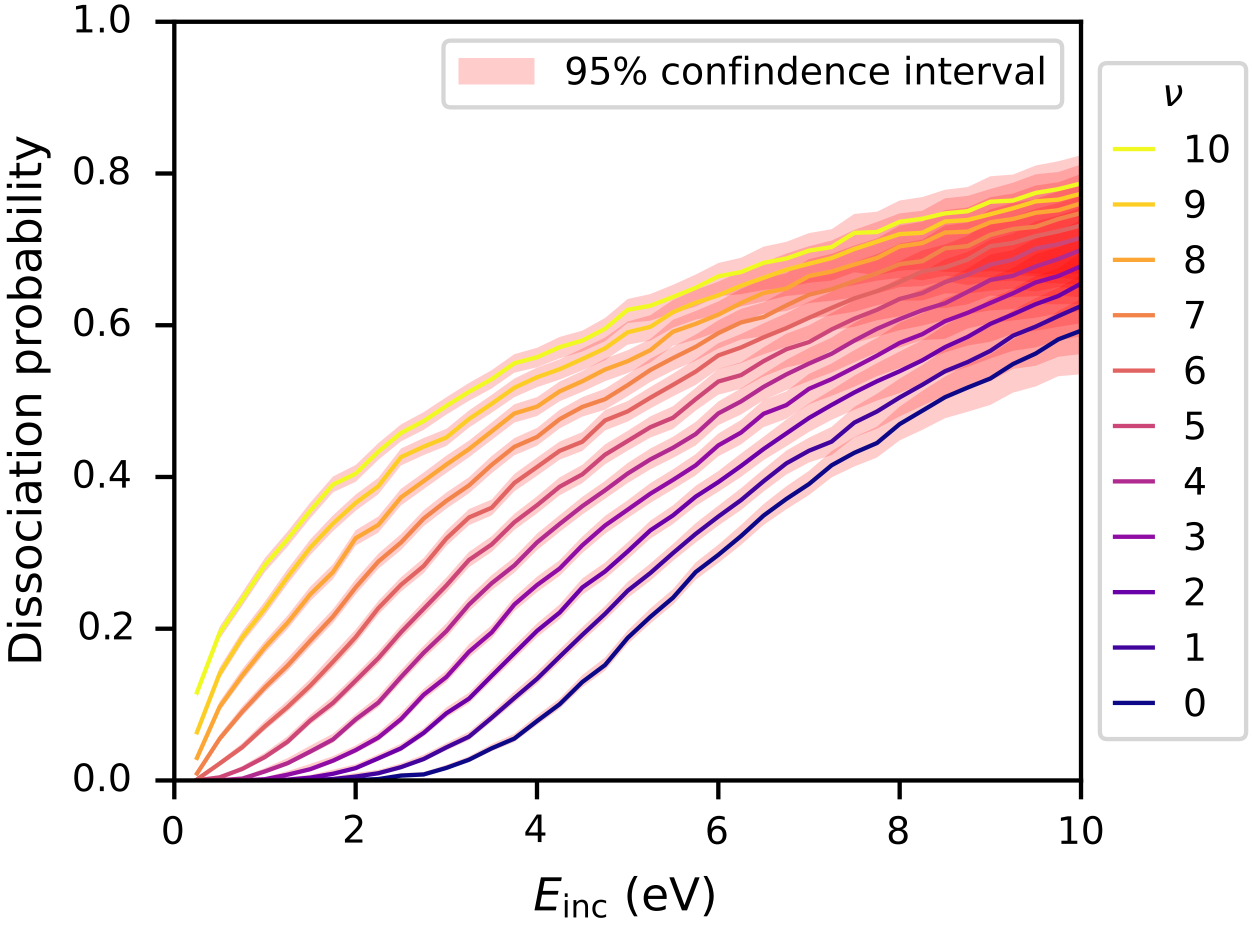

Figure S1: Dissociation probability curve dependent on incidence energy E_{inc} per vibrational quantum number ν. 95% confidence are indicated by the red shaded areas.

S2 Reaction probabilities under thermal conditions

S2.1 Methods relying on normal energy scaling

In Fig. 2, we show thermally-averaged reaction probabilities of N_2 DC on Ru(0001) based on our MD simulations. Taking the thermal average of the reaction probability curves requires computing the semi-infinite integral in Eq. (7) and requires reaction probability curves $P_\nu(E_\mathrm{inc})$ computed from MD (see Section S1). However, the numerical integration of the reaction probability poses some problems: The reaction probability $P_\nu(E_\mathrm{inc})$ quickly approaches 0 for $E_\mathrm{inc} \to 0$, while distribution (8) is heavily weighted towards $E_\mathrm{inc} \to 0$. This means that Monte Carlo sampling according to the Maxwell-Boltzmann distribution would require computing an intractable amount of trajectories ($\gg 10^6$). Instead, we compute the reaction curve $P_\nu(E_\mathrm{inc})$ at discrete values of $E_\mathrm{inc} = 0.25$–$10\,\mathrm{eV}$ in steps of $\Delta E_\mathrm{inc} = 0.25\,\mathrm{eV}$. Choosing initial conditions as detailed in Section 2.3.2, we assume that $P_\nu(E_\mathrm{inc})$ does not (significantly) depend on velocity components parallel to the surface, which is justified by normal energy scaling of

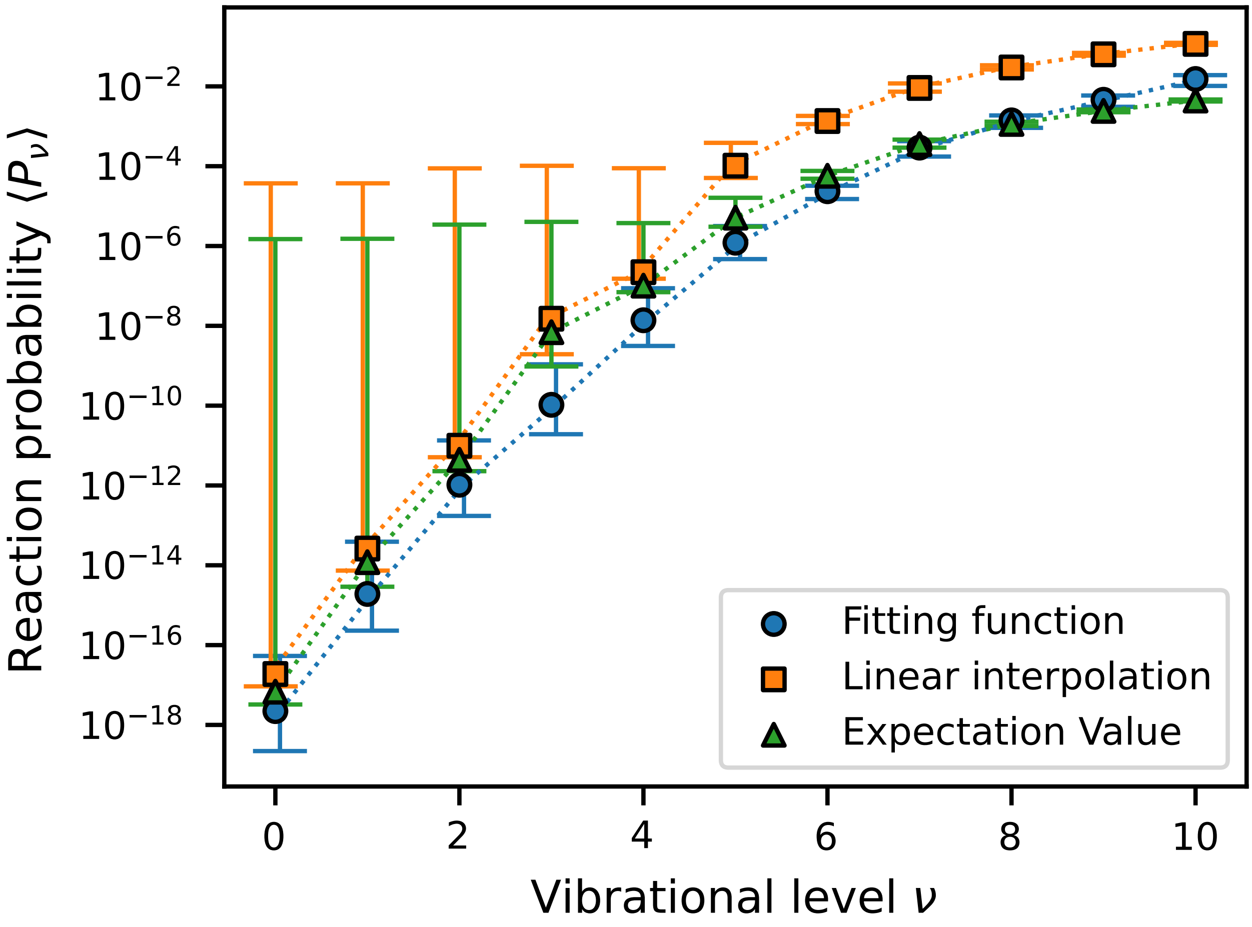

Figure S2: Comparison of methods for computing thermally averaged reaction probabilities as shown in Fig. 2 of the main article at $T_\mathrm{gas} = 673\,\mathrm{K}$.

N_2 dissociation probabilities on Ru(0001).[1] We use these reaction curves to approximate the integral given by Eq. (7). For this approximation, we used three methods:

1. Computing the expectation value with the sum

$$\langle P_\nu \rangle \approx \sum_{E_{\mathrm{inc}}} \left(\int_{E_{\mathrm{inc}}-\Delta E_{\mathrm{inc}}/2}^{E_{\mathrm{inc}}+\Delta E_{\mathrm{inc}}/2} f_{\mathrm{inc}}(\epsilon)\, \mathrm{d}\epsilon \right) P_\nu(E_{\mathrm{inc}}) \,. \tag{S1}$$

2. Computing the integral with a linearly interpolated reaction curves $g_\nu^1(E_{\mathrm{inc}})$ of the discrete reaction probabilities $P_\nu(E_{\mathrm{inc}})$ as

$$\langle P_\nu \rangle = \int_0^\infty f_{\mathrm{inc}}(E_{\mathrm{inc}})\, g_\nu^1(E_{\mathrm{inc}})\, \mathrm{d}E_{\mathrm{inc}} \,. \tag{S2}$$

3. Using a carefully constructed fitting function as given by Eq. (10), namely:

$$S_\nu(E) = \gamma_\nu \exp\left[-\beta_\nu E^{-\alpha_\nu}\right] \,, \tag{S3}$$

   and computing the integral

$$\langle P_\nu \rangle = \int_0^\infty f_{\mathrm{inc}}(E_{\mathrm{inc}})\, S_\nu(E_{\mathrm{inc}})\, \mathrm{d}E_{\mathrm{inc}} \,. \tag{S4}$$

   Here S_ν is the function $S(E)$ with optimal parameters $\alpha_\nu, \beta_\nu, \gamma_\nu$ obtained with a least-squares fit to $P_\nu(E_{\mathrm{inc}})$. These optimal parameters are reported in Section S2.1.

All three methods result in the same trend over the vibrational levels and are within 3 orders of magnitude of each other, as can be seen in Fig. S2. The results of the expectation value and the linear interpolation show consistent large upper bounds for $\nu < 6$. This upper bound is entirely determined by the number of trajectories and represents the maximum possible reaction probability when none of the trajectories have reacted, resulting in a roughly constant value. This observation led us to believe that it overestimates the true uncertainty. Therefore, we consider method 3 to be the best choice, as it provides a more consistent confidence interval across different vibrational levels.

ν	95% lower bound			Estimator			95% upper bound		
	α_ν	β_ν	γ_ν	α_ν	β_ν	γ_ν	α_ν	β_ν	γ_ν
0	1.99(11)	37.3(46)	0.815(54)	1.817(93)	30.4(32)	0.948(68)	1.586(79)	23.1(19)	1.167(92)
1	1.719(93)	20.4(19)	0.853(57)	1.561(83)	17.4(14)	1.000(73)	1.347(71)	13.92(85)	1.25(10)
2	1.437(77)	11.74(75)	0.930(63)	1.302(69)	10.55(55)	1.101(82)	1.120(59)	9.07(34)	1.39(12)
3	1.274(69)	7.96(37)	0.956(63)	1.138(61)	7.34(27)	1.149(85)	0.964(52)	6.58(16)	1.47(13)
4	1.039(57)	5.38(14)	1.068(76)	0.916(49)	5.183(98)	1.32(11)	0.775(39)	4.945(69)	1.71(15)
5	0.776(41)	3.929(64)	1.32(11)	0.684(34)	4.000(71)	1.68(15)	0.600(27)	4.036(83)	2.13(20)
6	0.600(27)	3.185(78)	1.58(12)	0.552(23)	3.315(82)	1.90(15)	0.524(19)	3.331(83)	2.10(16)
7	0.485(30)	2.70(10)	1.74(19)	0.422(27)	2.95(13)	2.34(30)	0.388(25)	3.06(14)	2.78(38)
8	0.414(29)	2.35(12)	1.79(21)	0.352(27)	2.66(15)	2.52(38)	0.325(25)	2.78(17)	2.99(50)
9	0.366(30)	2.05(13)	1.77(23)	0.298(28)	2.44(19)	2.67(49)	0.272(27)	2.60(21)	3.24(68)
10	0.280(32)	2.05(20)	2.17(42)	0.204(30)	2.73(35)	4.4(15)	0.177(29)	3.06(45)	6.3(28)

Table S1: Best fit parameters obtained for $S_\nu(E)$ (see Eq. (10) and also Eq. (S3) above) using the MD data for the reaction probability curves show in Fig. S1. We report fit parameters for the estimators as well as the 95% confidence interval upper and lower bounds.

S2.2 Direct sampling of Maxwell-Boltzmann distributions

Kedalo *et al.*[2] have tried to sample the thermal distribution for the impinging N_2 molecules directly. In Fig. S3 we compare their thermally averaged reaction probabilities for $T_{\text{gas}} = 1000\,\text{K}$ with results from our MD simulations as a function of vibrational state ν. Thanks to our fitting function we could simply re-evaluate Eq. (S4) without having to run additional MD simulations — which is another advantage of our method.

Figure S3 illustrates that the two sets of results for $\langle P_\nu \rangle$ differ greatly from each other. Unfortunately, Kedalo *et al.*[2] do not report statistical errors. They indicate to rely on an assumption for the initial velocities, namely that the "*z component (perpendicular to the surface) of the velocity was a minimum 80% of the total velocity*".[2] In the following we demonstrate that if statistical convergence has been achieved in their work, then it has been aided by this unphysical assumption. To do so, we first provide a rather general derivation of the skewed energy (E_z) and velocity (v_z) distributions f_{skew} used (according to our understanding) by Kedalo *et al.*[2] for sampling of initial velocities perpendicular to the surface at a given gas temperature T_{gas}. After that we compare it to the conventional Maxwell-Boltzmann distribution Eq. (8) used in our work.

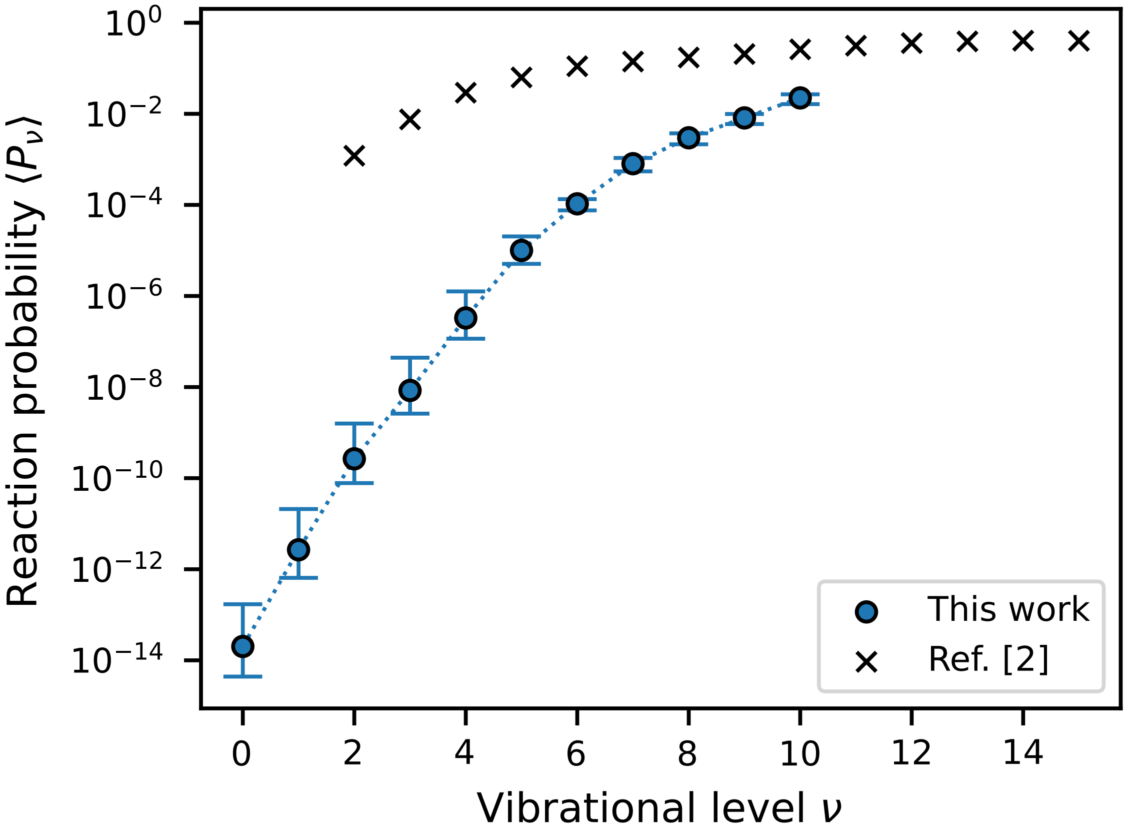

Figure S3: Comparison between thermal sticking probabilities of N_2 on Ru(0001) at $T_{\text{gas}} = 1000\,\text{K}$ computed in this work (blue circles) and Ref.[2] (black crosses).

Assuming that v_z is at least a fraction $0 < \xi < 1$ of the total velocity yields the following conditions:

$$\xi v_{\text{tot}} < v_z \tag{S5}$$

$$\xi^2 \tfrac{1}{2} m v_{\text{tot}}^2 < \tfrac{1}{2} m v_z^2 \tag{S6}$$

$$\xi^2 E_{\text{tot}} < E_z \tag{S7}$$

$$\xi^2 (E_x + E_y + E_z) < E_z \tag{S8}$$

$$\xi^2 (E_x + E_y) < (1 - \xi^2) E_z \tag{S9}$$

$$E_{\|} \equiv E_x + E_y < \frac{1-\xi^2}{\xi^2} E_z \tag{S10}$$

The kinetic energy contributions resulting from velocity components perpendicular and parallel to the surface are given by

$$E_z \sim \Gamma\left(\frac{1}{2}, k_{\text{B}} T_{\text{gas}}\right) \tag{S11}$$

and

$$E_{\|} \sim \Gamma\left(1, k_{\text{B}} T_{\text{gas}}\right) = \text{Exp}\left(\frac{1}{k_{\text{B}} T_{\text{gas}}}\right) , \tag{S12}$$

respectively. Up to a normalisation constant, the skewed energy distribution for the normal component is given by:

$$f_{\text{skew}}(E; T_{\text{gas}}) \propto P(E_z = E)\, P(E_{\|} < sE) \tag{S13}$$

$$\propto f_{\text{MB}-\text{1D}}(E; T_{\text{gas}})\; F_{\text{MB}-\text{2D}}(sE; T_{\text{gas}}) \tag{S14}$$

$$\propto \sqrt{\frac{1}{\pi k_{\text{B}} T_{\text{gas}} E}} \exp\left[\frac{-E}{k_{\text{B}} T_{\text{gas}}}\right] \left(1 - \exp\left[-s \frac{E}{k_{\text{B}} T_{\text{gas}}}\right]\right) , \tag{S15}$$

where $s = \frac{1-\xi^2}{\xi^2}$. $f_{\text{MB}-\text{1D}}$ denotes the probability distribution function of E_z, and $F_{\text{MB}-\text{2D}}$ denotes the cumulative distribution function of $E_{\|}$. Normalization yields

$$f_{\text{skew}}(E; T_{\text{gas}}) = \frac{1}{1 - \sqrt{\frac{1}{1+s}}} \sqrt{\frac{1}{\pi k_{\text{B}} T_{\text{gas}} E}} \exp\left[\frac{-E}{k_{\text{B}} T_{\text{gas}}}\right] \left(1 - \exp\left[-s \frac{E}{k_{\text{B}} T_{\text{gas}}}\right]\right) . \tag{S16}$$

Note that in the limit that $\xi \to 0$ (and thus $s \to \infty$) we recover Eq. (8) from Eq. (S16). The corresponding velocity distribution $\tilde{f}_{\text{skew}}$ is given by

$$\tilde{f}_{\text{skew}}(v; T_{\text{gas}}) = \frac{1}{2} m v\, f_{\text{skew}}\left(\frac{1}{2} m v^2\right) \tag{S17}$$

$$= \frac{1}{1 - \sqrt{\frac{1}{1+s}}} \sqrt{\frac{m}{2\pi k_{\text{B}} T_{\text{gas}}}} \exp\left[\frac{-m v^2}{2 k_{\text{B}} T_{\text{gas}}}\right] \left(1 - \exp\left[-s \frac{m v^2}{2 k_{\text{B}} T_{\text{gas}}}\right]\right) \tag{S18}$$

In Fig. S4 we have plotted $\tilde{f}_{\text{skew}}(v; T_{\text{gas}} = 1000\,\text{K})$ for $\xi = 80\,\%$ (i.e., $s = 0.5625$) together with the conventional (one-dimensional) Maxwell-Boltzmann velocity distribution. At this temperature, the severity of the skewness becomes very obvious.

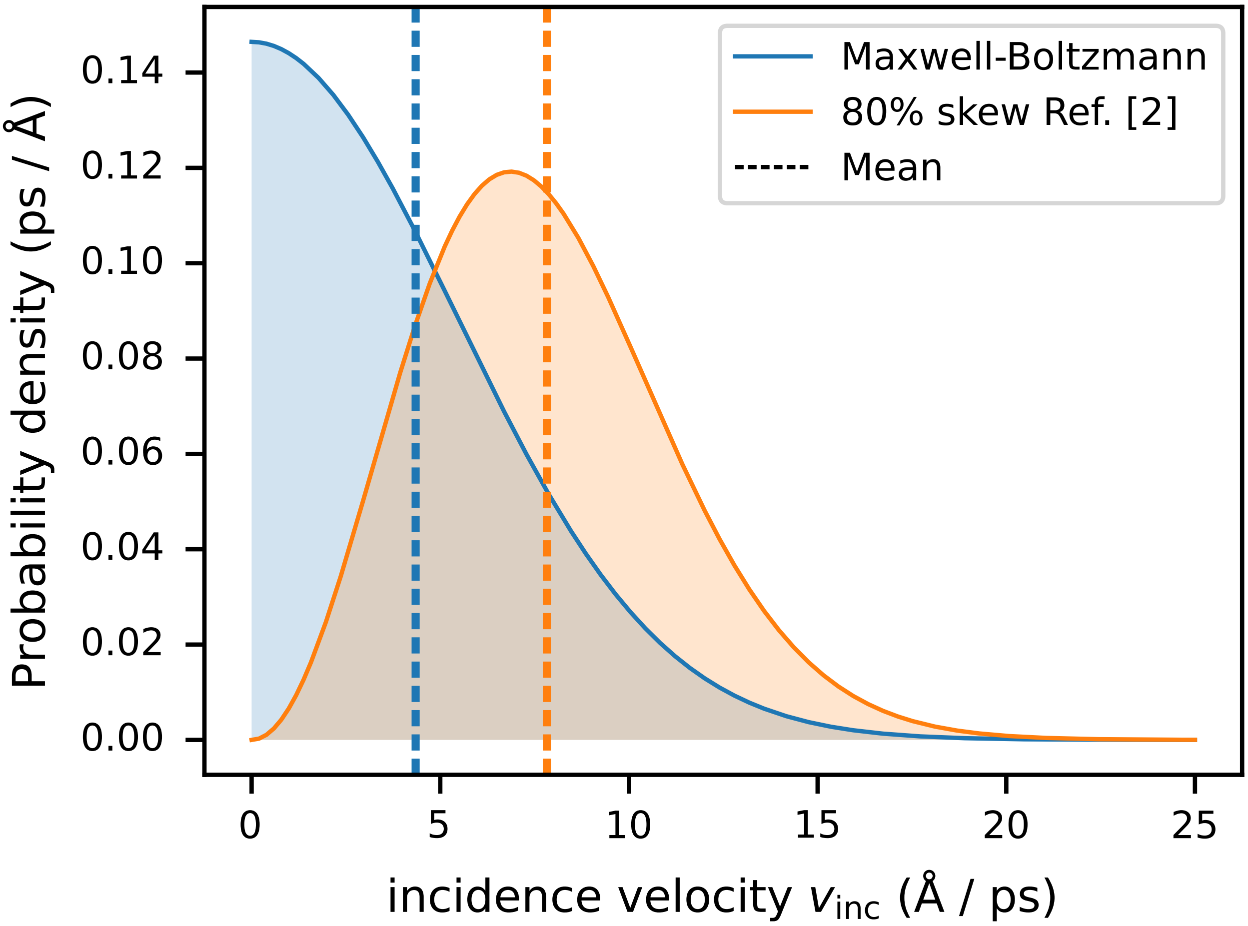

Figure S4: Comparison of velocity distributions at $T_{\mathrm{gas}} = 1000\,\mathrm{K}$: Conventional one-dimensional Maxwell-Boltzmann velocity distribution used in our work, skewed velocity distribution $\tilde{f}$ (see Eq. (S17)) resulting from the assumption that "*z component (perpendicular to the surface) of the velocity was a minimum 80% of the total velocity*"[2] (orange).

S3 Vibrational contributions

The turnover frequencies (TOFs) and reaction probabilities of Fig. 1 and Fig. 2 were computed using the rate coefficients (Eq. (6)). However, from these quantities, one cannot discern which vibrational states ν and incidence energies E_{inc} are the most relevant for the eventual rate of DC. The contribution $p_\nu(E_{\mathrm{inc}})$ of vibrational level ν at incidence energy E_{inc} is given by

$$p_\nu(E_{\mathrm{inc}}) = f_{\mathrm{vib}}(\nu)\, f_{\mathrm{inc}}(E_{\mathrm{inc}})\, P_\nu(E_{\mathrm{inc}})\,. \tag{S19}$$

Here, f_{vib} is the vibrational distribution given by a Boltzmann distribution (thermal) or by the Treanor distribution (Eq. (1)) (plasma); $f_{\mathrm{inc}}(E_{\mathrm{inc}})$ is the incidence energy distribution given by a 1D Maxwell-Boltzmann distribution; and $P_\nu(E_{\mathrm{inc}})$ is the DC probability computed from MD (see Section S1).

In Fig. S5a,b we see that for a thermal gas the most contributing vibrational states are $\nu = 3$–6, whereas for a plasma the highest vibrational states contribute the most to the total reaction probability. Supposedly, vibrational states higher than $\nu = 10$ are still relevant in a plasma, although the employed Treanor distribution model breaks down for $\nu > 10$, predicting increasingly higher occupations. In the future, a vibrational distribution function suitable for plasmas and even higher vibrational quantum numbers is required to investigate this. Furthermore, the relevant incidence energy range shifts downwards with each higher vibrational state. In contrast, with respect to the total energy ($E_{\mathrm{inc}} + E_\nu - E_{\mathrm{ZPE}}$) in Fig. S5c,d, we see that the energy range shifts upwards with ν.

Unfortunately, for the thermal distribution in Fig. S5b, most of the contributions are at a lower total energy than the minimum barrier height $E_{\mathrm{b}} = 1.83\,\mathrm{eV}$ (average of1.6 eV), which likely indicates artificial zero-point energy (ZPE) leakage, a well-known issue for the quasi-classical trajectory (QCT) approach that requires inclusion of nuclear quantum effects to remedy.[3] However, leakage of the ZPE (0.15 eV) alone is not enough to explain the discrepancy of$\sim$0.2 eV. A part of this discrepancy is also likely caused by the effective lowering of the local barrier height due to thermal surface atom motion. Contrary to under thermal conditions, we see under plasma conditions in Fig. S5d that the reactivity is determined mostly by collisions with a total energy larger than the minimum energy barrier. Nevertheless, this does mean that the reactivity of the lowest vibrational states is overestimated due to ZPE violation. This in turn affects the reaction rate of the vibrational ground state the most, followed by the thermal distribution, whereas the plasma distribution is hardly affected. Therefore, we predict that if the ZPE violation is solved in the molecular dynamics (MD) simulations (e.g., employing ring polymer MD simulations[3]), the differences between the computed TOFs of the three vibrational distributions are to become even larger, especially compared to the plasma distribution.

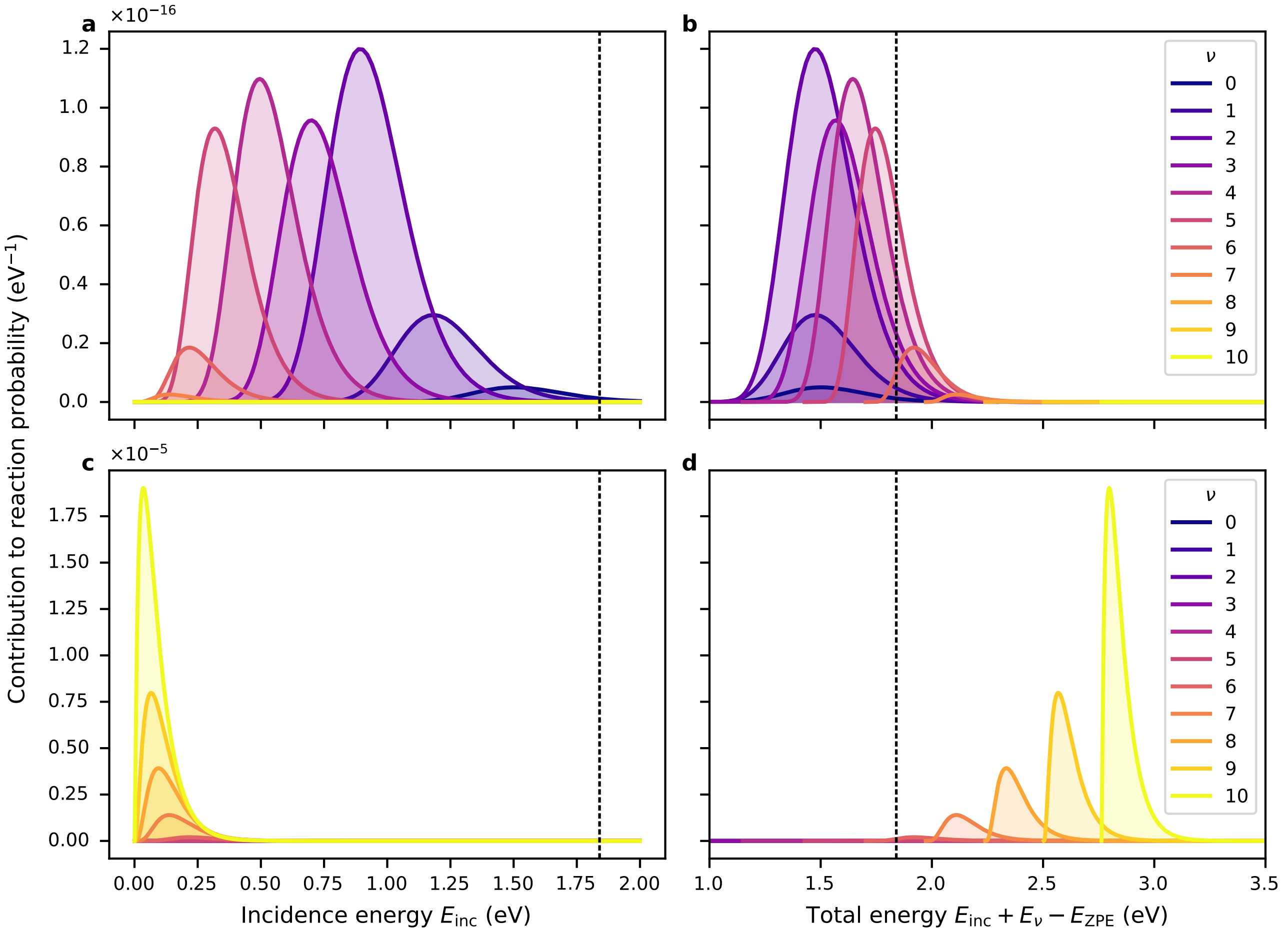

Figure S5: Relative contributions to the reaction probabilities of N_2 molecules pre-populated in different initial vibrational states ν according to a Boltzmann distribution ($T_{\mathrm{gas}} = 683\,\mathrm{K}$) for thermal catalysis (**a** and **b**) and Treanor distribution ($T_{\mathrm{gas}} = 683\,\mathrm{K}, T_{\mathrm{vib}} = 3000\,\mathrm{K}$) for plasma catalysis (**c** and **d**). **a** and **c** are plotted as a function of incidence energy E_{inc}, whereas **b** and **d** are as a function of total energy. The dashed lines indicate the minimum energy barrier $E_{\mathrm{b}} = 1.83\,\mathrm{eV}$.

S4 Mean vibrational efficacies

As described in Section 3.3, we compute a mean vibrational efficacy $\overline{\eta}$ from relative shifts $\delta E^{\nu}_{\text{inc}}$ between fitted reaction probability curves, that combine into total shifts w.r.t the ground state $\Delta E^{\nu}_{\text{inc}}$. Here we detail on the error estimation of the mean vibrational efficacy $\overline{\eta}$ and the goodness of this fit. For the practical implementation of the minimisation of Eq. (13), we interpolate the reaction curve integrals using a cubic spline. We evaluate the residuals between the two curves at 1024 points only on the overlap of the two data ranges after shifting to avoid extrapolation. The standard errors on the total shifts $\Delta E^{\nu}_{\text{inc}}$ are given by the root cumulative quadratic sum

$$\sigma_{\nu} = \sqrt{\sum_{i}^{\nu} C_{ii}}\,, \tag{S20}$$

where C_{ii} is the variance of δE_{inc} as given by the estimated covariance matrix C from the least-squares procedure. Note that the least-squares procedure is not weighted with the uncertainties of the reaction probability curves. These uncertainties are used in the weighted least-squares fit for $\overline{\eta}$. In the weighted least-squares, we fit the slope between the energy shifts $\Delta E^{\nu}_{\text{inc}}$ and corresponding vibrational excitation energies $\Delta E^{\nu}_{\text{vib}}$. We only fit the slope, enforcing that the linear fit goes through the reference point $(\Delta E^{\nu=0}_{\text{inc}}, \Delta E^{\nu=0}_{\text{vib}}) = (0, 0)$. The estimate for the mean vibrational efficacy follows from the least-squares procedure:

$$\overline{\eta} = \frac{\sum_{\nu} \frac{\Delta E^{\nu}_{\text{vib}} \Delta E^{\nu}_{\text{inc}}}{\sigma_{\nu}^{2}}}{\sum_{\nu} \left(\frac{\Delta E^{\nu}_{\text{vib}}}{\sigma_{\nu}}\right)^{2}}\,, \tag{S21}$$

and the uncertainty $\overline{\eta}$ is estimated as

$$\sigma_{\overline{\eta}} = \frac{1}{\sqrt{\sum_{\nu} \left(\frac{\Delta E^{\nu}_{\text{vib}}}{\sigma_{\nu}}\right)^{2}}}\,. \tag{S22}$$

In Fig. S6, we give a visual representation of this procedure. Fig. S6a shows the reaction probability curves and indicates the total energy shift $\Delta E^{\nu}_{\text{inc}}$ between the first excited state and the ground state. In Fig. S6b, we have plotted the total energy shift versus the excitation energies and find that the relation is almost perfectly linear. More precisely, the reduced chi-square statistic of the linear fit is $\chi^{2}_{\text{red}} = 0.022$, indicating very low residuals and most likely an overestimation of the uncertainties σ_{ν}. This overestimation is probably due to the assumption that the individual shifts $\delta E^{\nu}_{\text{inc}}$ are independent, allowing the formulation of Eq. (S20).

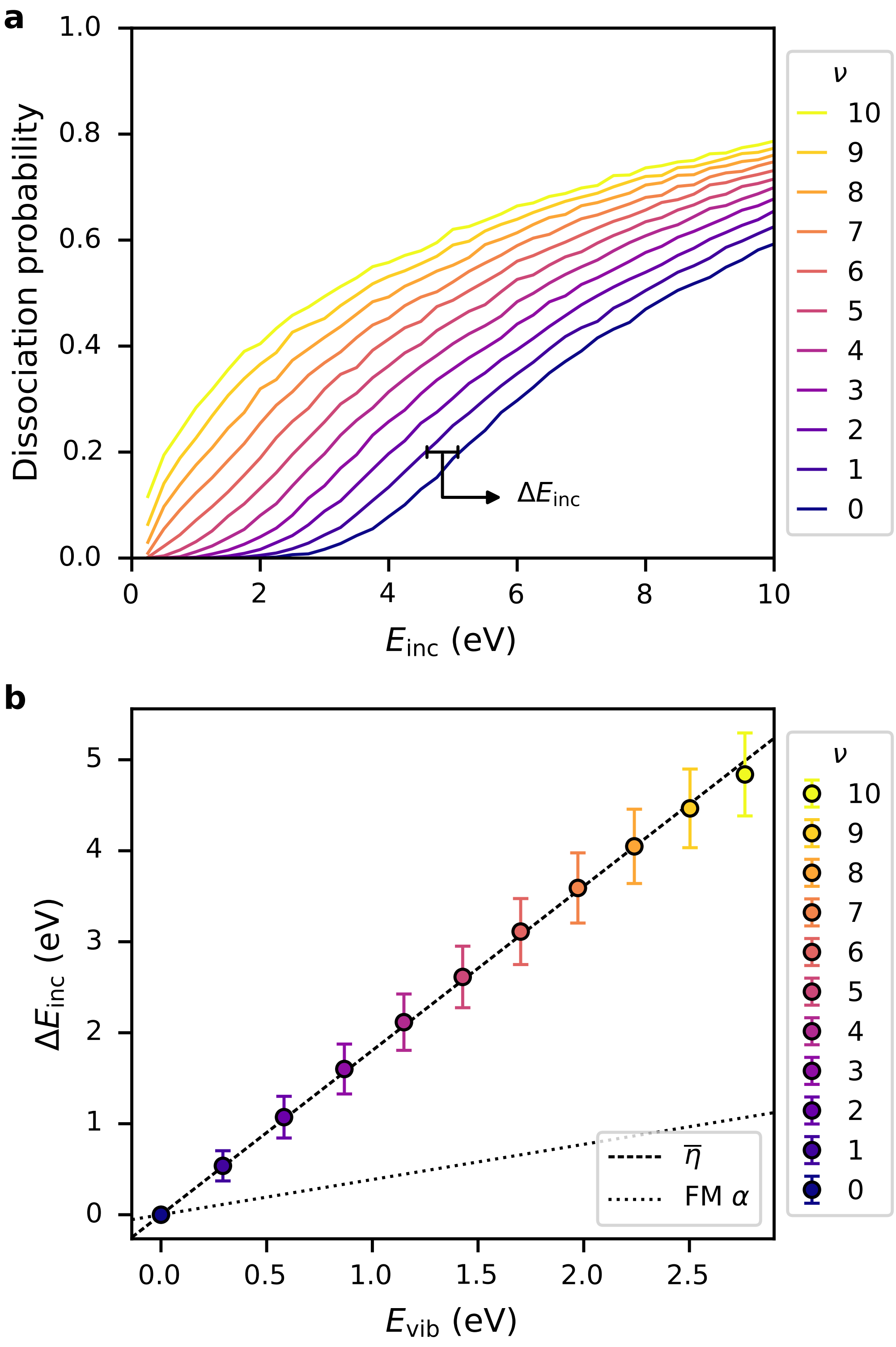

Figure S6: a) Reaction probability curves as function of incidence energy. b) Linear fit through the energy shifts $\Delta E^{\nu}_{\text{inc}}$ and excitation energies $\Delta E^{\nu}_{\text{vib}}$. The dashed line shows the linear fit corresponding to the mean vibrational efficacy $\overline{\eta}$ as used in the TST+$\overline{\eta}$@TS level of theory in the main article. The dotted line indicates the slope from FM α model (see Eq. (4)).

S5 Dynamical effects

As described in the main paper, we have computed the effect of the full-dimensional MD simulation on the DC probability on N_2 on Ru(0001). In (Section 3.4), we have also seen that the difference in reactivity of the MD simulations and TST-based methods can be explained by dynamical effects. We have shown the effects of the three most significant degrees of freedom (θ, x, y) in Fig. 4. The reduction in reactivity was computed by comparing the distribution of the initial coordinates for reacted trajectories and the thermal distributions of the N_2 molecule in the gas-phase. We will briefly describe these distributions here:

For the θ-angle, the thermal distribution is a sine distribution, given by the probability density function

$$f_{\text{thermal}}(\theta) = \tfrac{1}{2}\sin(\theta)\,. \tag{S23}$$

For the reacted trajectory distribution we slightly modified this distribution by multiplying it with a Gaussian centred around $\theta = \frac{\pi}{2}$ such that its probability density function is given by

$$f_{\text{reacted}}(\theta) = \frac{1}{N}\sin(\theta)\exp\left[-\left(\frac{\theta-\frac{\pi}{2}}{\sigma}\right)^2\right]\,, \tag{S24}$$

where σ is the standard deviation of the Gaussian and N is the normalisation constant, which is given by

$$N = \frac{\sqrt{\pi}}{2}\sigma\exp\left[-\frac{\sigma^2}{4}\right]\,\Re\left(\operatorname{erf}\left[\frac{\pi - i\sigma^2}{2\sigma}\right] + \operatorname{erf}\left[\frac{\pi + i\sigma^2}{2\sigma}\right]\right)\,, \tag{S25}$$

where $\Re$ denote the real part and erf the error function.

For the ϕ-angle, the thermal distribution is just a uniform distribution over the interval $[0, 2\pi)$. The distribution for the reacted trajectory was modelled by a uniform distribution mixed with a cosine distribution with probability density distribution

$$f_{\text{reacted}}(\phi) = \frac{1}{2\pi}[1 + \cos(k\phi)]\,. \tag{S26}$$

Here k denotes the number of maxima of the function, where we have chosen $k = 6$, because of the 3-fold and 2-fold symmetries of Ru(0001) and N_2, respectively. A similar distribution has been used in the work of Shakouri *et al.*[4].

For the xy-positions, the thermal distribution is again a uniform distribution, but now over the irreducible wedge of the Ru(0001) surface, as depicted in Fig. 4b. The reacted distribution is modelled by a bimodal normal distribution as the sum of two 2D Gaussians: The first is centred at $\mu_1 = (\frac{3}{4}a, \sqrt{\frac{3}{16}}a)$, which is the bridge site, and has inverse covariance matrix

$$\Sigma_1^{-1} = \frac{1}{4}\begin{pmatrix} 3a^2 + b^2 & \sqrt{3}(a^2 - b^2) \\ \sqrt{3}(a^2 - b^2) & a^2 + 3b^2 \end{pmatrix} = R(30^\circ)\begin{pmatrix} a^2 & 0 \\ 0 & b^2 \end{pmatrix} R^{-1}(30^\circ)\,. \tag{S27}$$

This means that the inverse principal variances a^2, b^2 are directed along the 30° symmetry axis of the reduced wedge. The second Gaussian is centred at $\mu_2 = (a, 0)$ with covariance, where the principal variances are in the same direction as Eq. (S27), but with independent inverse variance magnitudes c^2, d^2. The full probability density function is then given by

$$f_{\text{reacted}}(x, y) = e\, g_1(x, y) + (1 - e) g_2(x, y)\,, \tag{S28}$$

$$g_1(x, y) = \frac{ab}{\pi} \exp\left[-\tfrac{1}{2} d_1^T \Sigma_1^{-1} d_1\right]\,, \tag{S29}$$

$$g_2(x, y) = \frac{cd}{\arctan \frac{\sqrt{3}d}{c}} \exp\left[-\tfrac{1}{2} d_2^T \Sigma_2^{-1} d_2\right]\,, \tag{S30}$$

$$d_i = \begin{pmatrix} x \\ y \end{pmatrix} - \mu_i\,. \tag{S31}$$

In these equations, e is the mixture parameter between the two normal distribution, a^2, b^2 (c^2, d^2) are the inverse principal variances of the first (second) normal distribution. Note that this distribution is not exactly normalized when the distributions are very broad, as we approximated the distribution to vanish at opposite boundaries of the reduced wedge.

In Fig. S7 we show the reduction in reactivity from the MEP deviations beyond the example at an incidence energy of $E_{\text{inc}} = 3.25\,\text{eV}$ presented in Fig. 4. From this figure, we can recover the ranges of reduction reported in the main paper and see that the reduction from the angular degrees of freedom stays approximately constant as a function of incidence energy, while the reduction associated with the translational degrees of freedom decreases with incidence energy. Assuming that these degrees of freedom are completely independent is not realistic. For example, we know that the optimal azimuthal angle ϕ is sensitive to the position x, y.[4] Regardless, even if the degrees of freedom are perfectly correlated, the minimal reduction would be due to corrugation in x, y, which still accounts for a reduction in reactivity of almost two-orders-of-magnitude. Furthermore, from the trend we believe that this reduction becomes even larger for incidence energies $E_{\text{inc}} < 1.75\,\text{eV}$, which are beyond our statistics for this particular analysis and are required to determine both thermal and plasma catalysis reaction rates (see Fig. S5a,c).

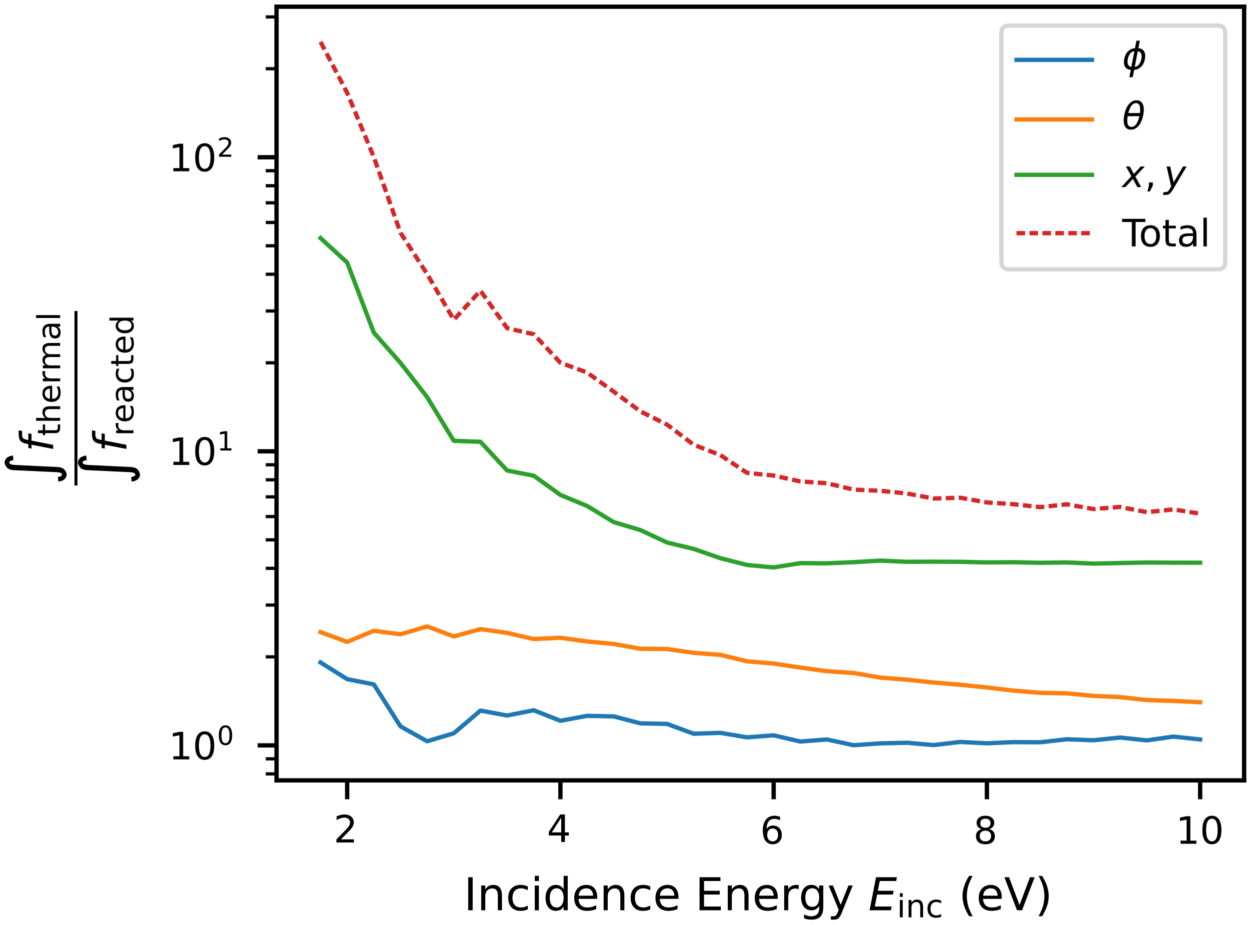

Figure S7: Reactivity reduction of MD with respect to TST-based methods obtained from difference in distributions described in Section S5 and shown in Fig. 4.

S6 Barrier recrossing

As mentioned in Section 3.4, in MD there is a possibility for a single N_2 molecule to cross the reaction barrier multiple times, which is erroneously counted multiple times towards the reaction rate in TST. We quantify this recrossing rate by performing an additional 5000 QCTs and counted how often the bond length of N_2 crossed its transition state value $r^{\ddagger} = 1.738\,\text{Å}$. As the barrier for the DC of N_2 on Ru(0001) is a late barrier, crossing $r^{\ddagger}$ closely coincides with the actual transition state plane. In Fig. S8, we can see that the probability of crossing the transition state decreases exponentially with the number of crossings. Only a small amount of trajectories actually recross the barrier ($\sim 5\,\%$ at $E_{\text{inc}} = 5.0\,\text{eV}$ and $\nu = 0$). The overestimation of the dissociation rate in TST due to recrossing is usually accounted for by a transmission coefficient κ that quantifies how often a crossing of the transition state leads to dissociation. This transmission coefficient is given by the ratio between the number of dissociations and transition state crossings as

$$\kappa = \frac{N_{\text{diss}}}{N_{\text{cross}}}\,. \tag{S32}$$

Here N_{cross} is the total number of crossing (forward and backward) over all trajectories and N_{diss} is the number of trajectories that ended in dissociation. The overestimation coefficient κ is thus dependent on the incidence energy E_{inc} and vibrational state ν. In Fig. S9 we show the that the overestimation of the reaction probability for $\nu = 0$ is10–20 %. However, for realistic catalytic conditions, the relevant incidence energies are lower than2 eV, where we do not observe recrossing. Thus, recrossing can be neglected for computing the reaction rate of N_2 + Ru(0001) with TST models.

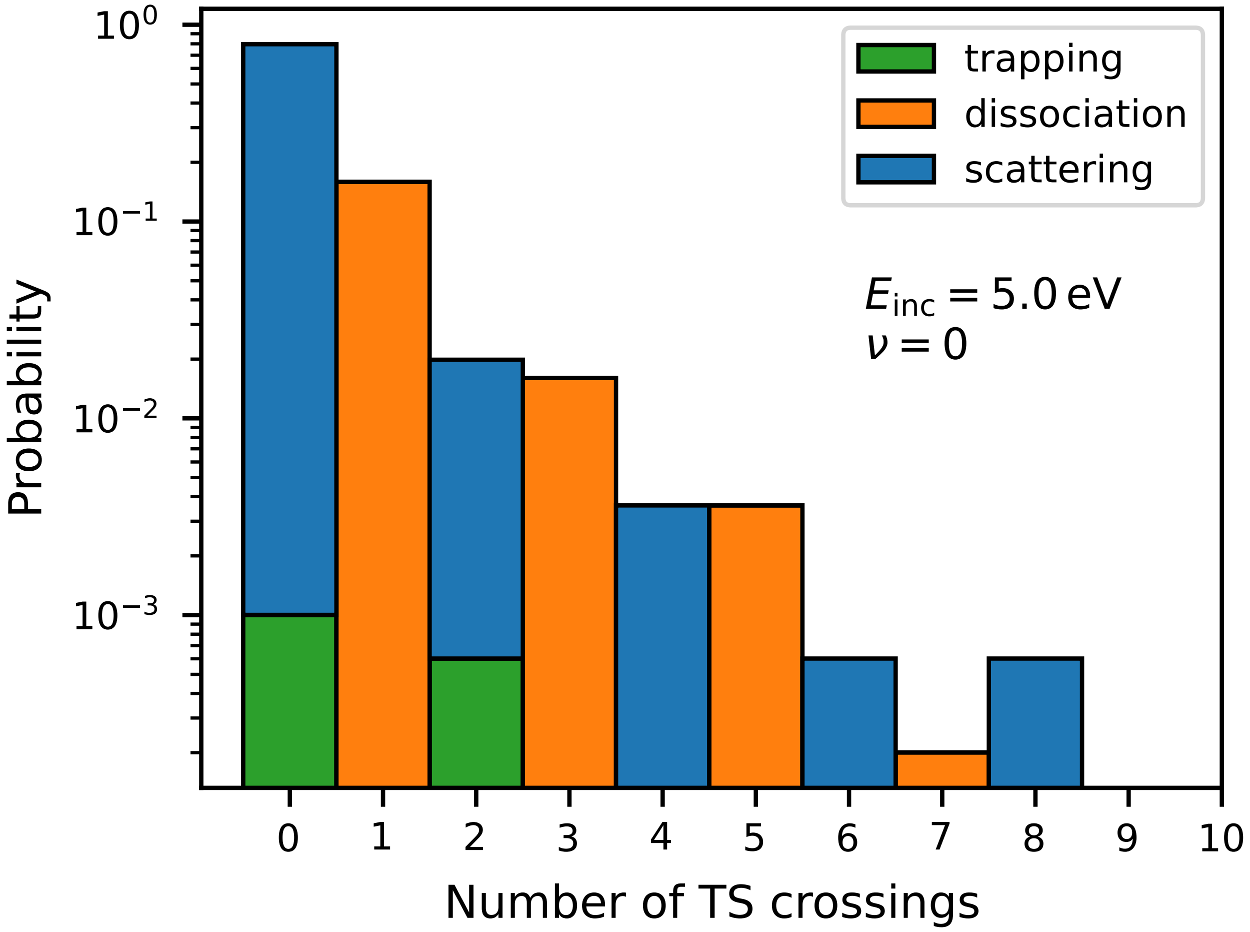

Figure S8: Distribution of the number of crossings of the molecule over the transition plane for scattered (blue), dissociated (orange) and trapped trajectories (green). The plot is for an incidence energy of $E_{\mathrm{inc}} = 5.0\,\mathrm{eV}$ in the vibrational ground state $\nu = 0$ using the technical parameters for recrossing defined in Section S6.

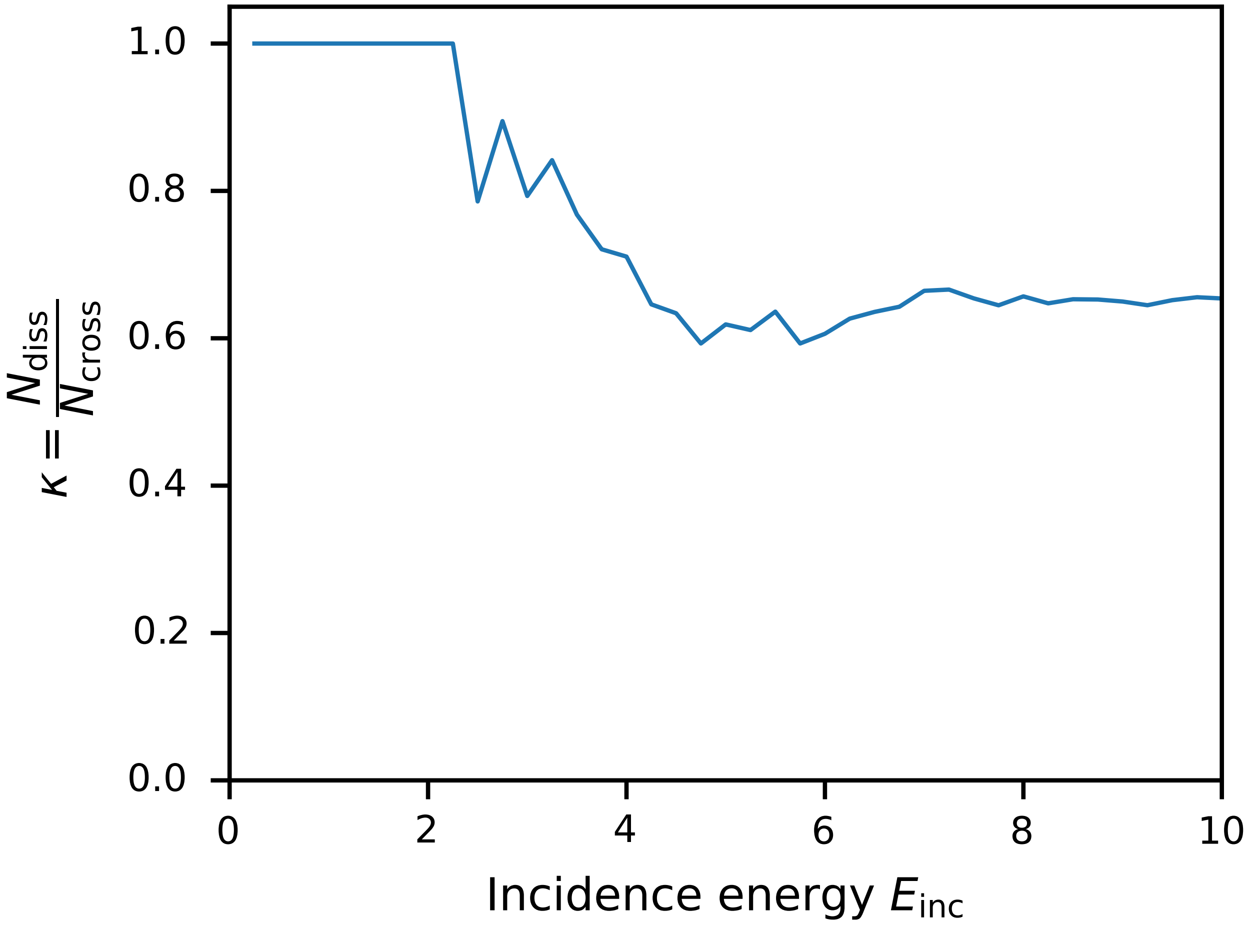

Figure S9: Transmission coefficient of DC derived from barrier recrossings. The transmission coefficients κ shown here are computed from QCTs in vibrational state $\nu = 0$.

References

[1] D. Seets, M. Wheeler and C. Mullins, Kinetics and Dynamics of Nitrogen Adsorption on Ru(001): Evidence for Direct Molecular Chemisorption, *Chem. Phys. Lett.*, 1996, **257**, 280–284, DOI: 10.1016/0009-2614(96)00542-8.

[2] Y. M. Kedalo, A. A. Knizhnik and B. V. Potapkin, Applicability of the Fridman–Macheret α-Model to Heterogeneous Processes in the Case of Dissociative Adsorption of N_2 on the Ru Surface, *J. Phys. Chem. C*, 2023, **127**, 11536–11541, DOI: 10.1021/acs.jpcc.3c01967.

[3] N. Gerrits, B. Jackson and A. Bogaerts, Accurate Reaction Probabilities for Translational Energies on Both Sides of the Barrier of Dissociative Chemisorption on Metal Surfaces, *J. Phys. Chem. Lett.*, 2024, 2566–2572, DOI: 10.1021/acs.jpclett.3c03408.

[4] K. Shakouri, J. Behler, J. Meyer and G.-J. Kroes, Analysis of Energy Dissipation Channels in a Benchmark System of Activated Dissociation: N_2 on Ru(0001), *J. Phys. Chem. C*, 2018, **122**, 23470–23480, DOI: 10.1021/acs.jpcc.8b06729.